

## Fermiology and type-I superconductivity in the chiral superconductor NbGe<sub>2</sub> with Kramers-Weyl fermions

Eve Emmanouilidou,<sup>1</sup> Sougata Mardanya,<sup>2,3</sup> Jie Xing,<sup>1</sup> P. V. Sreenivasa Reddy ,<sup>2</sup> Amit Agarwal,<sup>3</sup> Tay-Rong Chang,<sup>2,4,5,\*</sup> and Ni Ni <sup>1,†</sup>

<sup>1</sup>*Department of Physics and Astronomy and California NanoSystems Institute, University of California, Los Angeles, Los Angeles, California 90095, USA*

<sup>2</sup>*Department of Physics, National Cheng Kung University, Tainan 701, Taiwan*

<sup>3</sup>*Department of Physics, Indian Institute of Technology, Kanpur 208016, India*

<sup>4</sup>*Center for Quantum Frontiers of Research and Technology, Tainan 701, Taiwan*

<sup>5</sup>*Physics Division, National Center for Theoretical Sciences, Hsinchu 300, Taiwan*



(Received 28 August 2020; accepted 17 November 2020; published 21 December 2020)

In this paper we present a systematic study of the de Haas–van Alphen (dHvA) oscillations, magnetotransport, and superconductivity in the Kramers-Weyl semimetal candidate NbGe<sub>2</sub>. We show that NbGe<sub>2</sub> is a type-I chiral superconductor with a  $T_c$  of 2.06 K, a full gap, a type-II to type-I crossover around 1.5 K, and an enhanced critical field from filamentary superconductivity suggested by resistivity measurements. The study of the dHvA oscillations reveals three distinct frequency branches  $\beta$  and the spin-split  $\alpha/\alpha'$ , with cyclotron effective masses of  $1.21(5)m_e$ ,  $0.21(1)m_e$ , and  $0.24(1)m_e$ , respectively. The magnetoresistance of NbGe<sub>2</sub> exceeds 1000% at 2.4 K and 9 T and exhibits quasilinear behavior at low temperatures. The comparison between experimental results and first-principles calculations shows excellent agreement between the two and suggests that  $\alpha$  and  $\alpha'$  correspond to the hole Fermi pockets centered around the Weyl  $M$  point, while  $\beta$  is associated with the hole pocket near the trivial  $H$  point in the Brillouin zone. Furthermore, we show that a Van Hove singularity arising from the contributions of the  $M$  and  $H$  points at the Fermi level, together with the calculated electron-phonon coupling, is strong enough to account for the observed superconductivity. Last, our calculation of the conductivity tensor within the relaxation time approximation suggests that the observed linear magnetoresistance most likely arises from the presence of open Fermi surfaces.

DOI: [10.1103/PhysRevB.102.235144](https://doi.org/10.1103/PhysRevB.102.235144)

### I. INTRODUCTION

The discovery of topologically protected conducting surface states in three-dimensional (3D) topological insulators [1,2] inspired remarkable interest in topological materials. Predictions for the existence of topological semimetals followed shortly after [3]. These materials host low-energy quasiparticle excitations with linear dispersion relations that are similar to the elusive relativistic fermions predicted by elementary particle physics, with Dirac and Weyl fermions being the most prominent examples. The successful material realizations of such topological semimetals and the progressive understanding of the role of band topology in physical properties have led to the discoveries of surface Dirac cones [4], surface Fermi arcs [5], and the chiral anomaly [6] and colossal photovoltaic effects [7], to name a few.

A new addition to the class of topological semimetals is the Kramers-Weyl semimetal [8]. Topological insulators and semimetals are characterized by band crossings that are protected by crystalline or time-reversal symmetries.

In nonmagnetic chiral crystals which have only pure rotational symmetries, spin-orbit coupling (SOC) splits the doubly degenerate bands everywhere except at the time-reversal invariant momenta (TRIMs), where the bands must remain doubly degenerate according to Kramers's theorem. These crossings are characterized by a quantized chiral charge and were thus termed Kramers-Weyl fermions [8]. NbGe<sub>2</sub> was predicted to belong to this new class of Kramers-Weyl semimetals. Additionally, studies dating back to the 1970s found that it becomes superconducting (SC) at low temperatures, although the reported  $T_c$  ranged from 2 K in single crystals to 16 K in sputtered films [9,10]. In noncentrosymmetric superconductors (NCSs), the lack of an inversion center and the presence of antisymmetric spin-orbit coupling (ASOC) can lead to an admixture of spin-singlet and spin-triplet states [11]. Previously discovered NCSs exhibit a wide range of behaviors, with some showing evidence of unconventional SC [12] and others being fully gapped  $s$ -wave SCs [13]. The presence of nontrivial band topology coupled with SC properties makes NbGe<sub>2</sub> a candidate for chiral topological SC.

In this paper, we present our results on the single-crystal growth, thermodynamic, magnetotransport, and torque measurements, as well as first-principles calculations for NbGe<sub>2</sub>.

\*Corresponding author: [u32trc00@phys.ncku.edu.tw](mailto:u32trc00@phys.ncku.edu.tw)

†Corresponding author: [nini@physics.ucla.edu](mailto:nini@physics.ucla.edu)

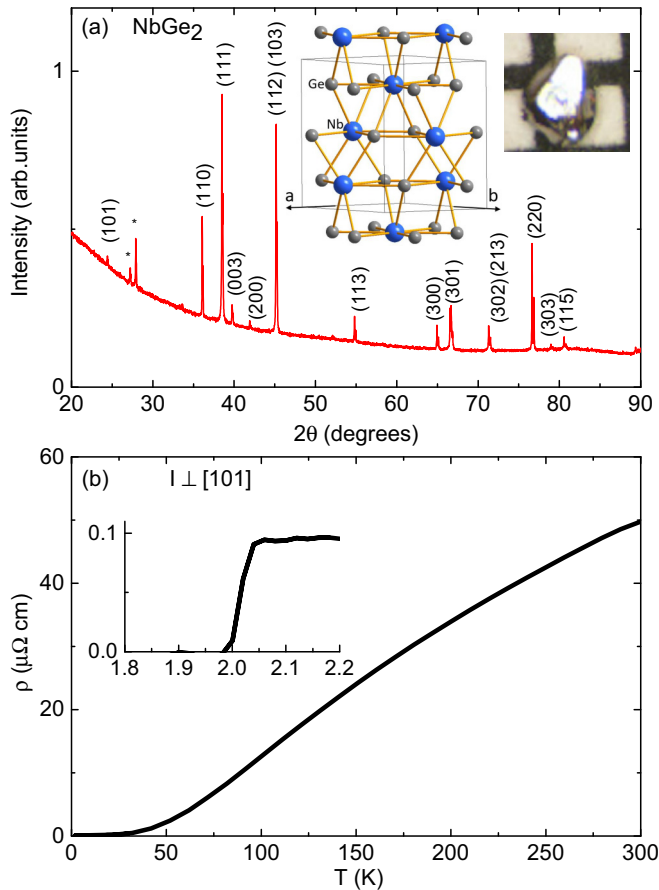


FIG. 1. (a) The powder x-ray diffraction pattern of NbGe<sub>2</sub>. The peaks with asterisks are due to impurities, most likely due to Ge flux. The crystal structure and a picture of a single crystal against a millimeter background are shown in the insets. (b) The resistivity of a NbGe<sub>2</sub> single crystal at 0 T. Inset: zoomed-in plot of the superconducting transition.

## II. EXPERIMENTAL METHODS

Single crystals were grown using the self-flux method, with Ge being the flux. Nb powder was mixed with Ge pieces at a molar ratio of 6:94 and placed inside an alumina crucible which was in turn placed in a Ta tube. The tube was evacuated and filled with Ar gas before being sealed using an arc melter. The growth ampoule was subsequently placed in a vertical one-zone furnace that was flushed with Ar gas during the heat treatment. The ampoule was then heated to 1400 °C for 2 h and then slowly cooled to 900 °C at a rate of 3 °C/h. The furnace was shut down at 900 °C and allowed to cool down to room temperature. The alumina crucible was retrieved from the Ta tube and then sealed in a quartz tube. The ampoule was then placed into a preheated furnace at a temperature of 960 °C for 30 min, followed by a decanting of the liquid from the single crystals using a centrifuge. Small, but thick, high-quality 3D single crystals were obtained, as shown in the inset of Fig. 1.

Powder x-ray diffraction measurements were performed using a PANalytical Empyrean (Cu  $K\alpha$  radiation) diffractometer. The specific heat measurements were performed in a Quantum Design (QD) Dynacool physical property

measurement system (PPMS) with a maximum magnetic field of 9 T. Magnetic susceptibility measurements were performed in a QD vibrating-sample magnetometer magnetic property measurement system (MPMS3). Magnetic torque and magnetotransport measurements were performed inside a QD PPMS with a maximum magnetic field of 9 T. For the torque measurements, a small piece cut from a single crystal was mounted to the tip of a piezoresistive cantilever. The magnetic torque was then inferred from the magnetoresistance of the cantilever measured by a Wheatstone bridge, as the resistance of the cantilever is very sensitive to the deformation caused by torque. The electrical resistivity ( $\rho_{xx}$ ) and Hall ( $\rho_{yx}$ ) measurements were performed using the six-probe technique. To eliminate unwanted contributions from mixed transport channels, data were collected while sweeping the magnetic field from  $-9$  to  $9$  T. The data were then symmetrized to obtain  $\rho_{xx}(B)$  using  $\rho_{xx}(B) = [\rho_{xx}(B) + \rho_{xx}(-B)]/2$  and antisymmetrized to get  $\rho_{yx}(B)$  using  $\rho_{yx}(B) = [\rho_{yx}(B) - \rho_{yx}(-B)]/2$ . The sign of  $\rho_{yx}$  is chosen so that hole carriers lead to positive  $\rho_{yx}$ . The magnetoresistance is defined as  $MR = [\rho_{xx}(B) - \rho_{xx}(0)]/\rho_{xx}(B)$ .

The electronic structure calculations were carried out within the framework of density functional theory (DFT) [14,15], with the projector augmented wave pseudopotentials [16], as implemented in the Vienna Ab initio Simulation Package (VASP) [17,18]. The exchange-correlation effects were included within the generalized gradient approximation with the Perdew-Burke-Ernzerhof parametrization [19]. SOC effects were treated self-consistently to incorporate relativistic effects. To perform the electronic calculations, we used a plane-wave energy cutoff of 300 eV, while the Brillouin zone (BZ) sampling was done by a  $21 \times 21 \times 11$   $\Gamma$ -centered  $k$  mesh [20]. Total energies were converged to  $10^{-6}$  eV in combination with Gaussian-type broadening of 0.05 eV. The experimental lattice parameters were used in all calculations, while the ionic positions were relaxed until the residual force on each atom was less than  $10^{-3}$  eV/Å. The Fermi surface calculation was done by employing a tight-binding model obtained through the WASP2WANNIER90 interface [21], and visualization of the Fermi surface was done using the XCRYSDEN software.

## III. EXPERIMENTAL RESULTS AND DISCUSSION

NbGe<sub>2</sub> crystallizes in the CrSi<sub>2</sub>-type chiral noncentrosymmetric hexagonal crystal structure with the space group  $P6_222$ , as shown in the inset of Fig. 1, where each Nb atom is covalently bonded to six Ge atoms that lie on the vertices of a hexagon in the  $ab$  plane and four Ge atoms out of plane. The powder diffraction from crushed single crystals shows that our NbGe<sub>2</sub> can be well indexed by such a crystal structure [22]. Figure 1(b) presents the temperature-dependent resistivity of NbGe<sub>2</sub> from 300 to 2 K. The sample shows metallic behavior with a resistivity of 50  $\mu\Omega$  cm at room temperature and has a residual resistivity ratio (RRR), defined here as  $\rho(300 \text{ K})/\rho(2.2 \text{ K})$ , of 520. The high RRR and the sharp SC transition, shown in the inset of Fig. 1(b), are indicative of the high quality of the sample.

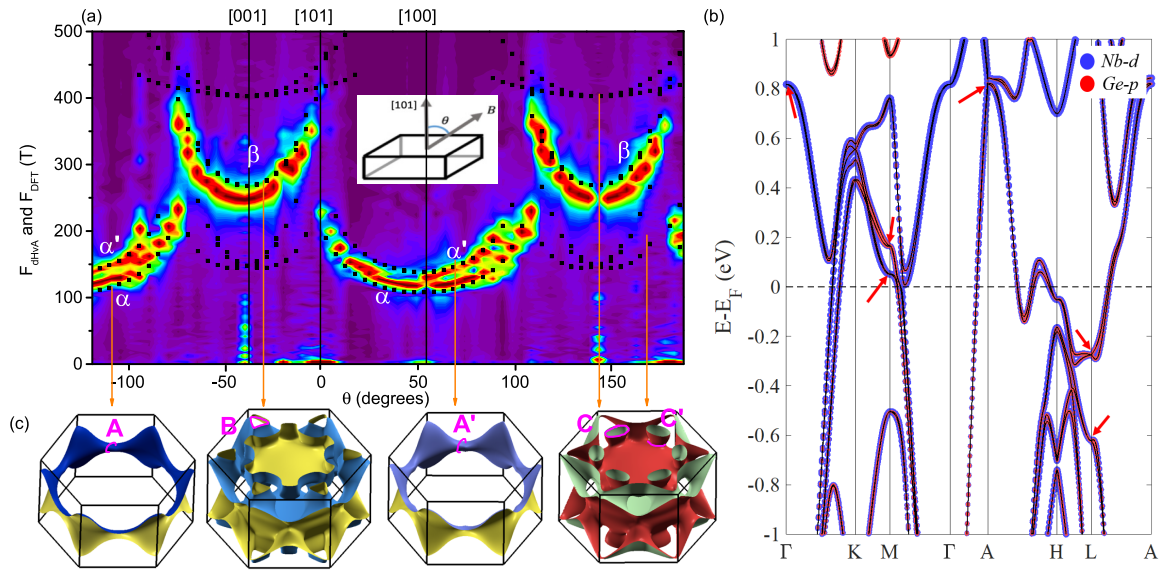


FIG. 2. (a) The contour plot of the FFT frequencies as a function of angle. Three frequency branches can be distinguished, labeled  $\alpha$ ,  $\alpha'$ , and  $\beta$ . Strong spin splitting is observed for  $\alpha$  and  $\alpha'$ . The black dots correspond to the DFT-calculated frequencies. The inset shows the measurement geometry. (b) The orbital-resolved electronic band structure of bulk NbGe<sub>2</sub> with SOC. The blue and red dots indicate Nb 4d orbitals and Ge 4p orbitals, respectively. The red arrows denote the positions of Weyl points. (c) The Fermi surfaces in the full BZ of NbGe<sub>2</sub>. The first three panels show holelike pockets, and the last panel shows an electron pocket. The extremal cross sections with oscillation frequencies less than 500 T are labeled A, A', B, C, and C'. From a comparison of dHvA and DFT, it is clear that the  $\alpha$ ,  $\alpha'$ , and  $\beta$  branches correspond to A, A', and B, respectively.

### A. Electronic structure revealed by quantum oscillations and DFT calculations

De Haas–van Alphen (dHvA) oscillations were observed in the magnetic torque, which is related to magnetization through equation  $\vec{\tau} = \vec{M} \times \vec{B}$ . The frequency of the oscillations  $F$  is related to the extremal cross-sectional area of the Fermi surface perpendicular to the applied magnetic field through the equation  $F = \frac{\hbar}{2\pi e} A$ . By rotating the sample about a crystallographic axis in a magnetic field, the angle-dependent dHvA frequencies can give us valuable information about the extremal cross sectional areas and thus the fermiology of a material.

Figure 2(a) shows a contour plot of the frequencies obtained using a fast Fourier transform (FFT) as a function of angle. The measurement geometry is shown in the inset, and the data were collected at 5° intervals. Three branches of dHvA frequencies  $F_{\text{dHvA}}$  were observed, which we assigned to three different Fermi pockets. The small difference in magnitude and similar angular dependences of  $\alpha$  and  $\alpha'$  suggest spin splitting of the electronic structure caused by ASOC. Since ASOC has the form of a Zeeman term but with a fictitious magnetic field that is momentum dependent, it lifts the twofold spin degeneracy in noncentrosymmetric materials, resulting in a spin-split Fermi surface. This behavior has also been observed in other noncentrosymmetric materials such as VSi<sub>2</sub> [23] but was too small to be discerned in the chiral Weyl semimetal CoSi [24].

DFT calculations were performed to examine the fermiology and compare the results with the experimental dHvA data. The orbital-projected electronic band structure of NbGe<sub>2</sub> obtained from DFT calculations along high-symmetry directions, with SOC taken into account, is shown in Fig. 2(b). The

different colors depict contributions from different orbitals while the size of the dots shows the actual contribution. It can be readily seen that several valence and conduction bands cross the Fermi energy, suggesting a metallic-type behavior with the major contributions to the band structure coming from the hybridization of the Nb 4d and Ge 4p orbitals near the Fermi energy. The band structure shows band splitting due to the breaking of spatial inversion symmetry, except at the TRIMs ( $\Gamma$ ,  $M$ ,  $A$ , and  $L$ ) of the BZ. Our calculation indicates that these gapless band crossings at the TRIMs marked by the red arrows in Fig. 2(b) are the Kramers-Weyl points, which is consistent with a recent publication [8]. The Weyl point at high-symmetry point  $M$  ( $\approx 0.05$  eV) is close to the Fermi energy and is expected to contribute relativistic electrons/holes near the Fermi level. Additionally, the band structure at  $M$  ( $\approx 0.05$  eV) and  $H$  ( $\approx -0.05$  eV) features a saddle-point-like dispersion near the Fermi level which eventually results in a Van Hove-type singularity in the density of states at the Fermi energy, which may be responsible for the observed SC.

The Fermi surface of NbGe<sub>2</sub> is shown in Fig. 2(c). Of the four Fermi pockets which comprise the Fermi surface, three are hole-type ones (first three panels), and one is electron type (fourth panel). With the magnetic field rotating away from the [101] axis, we computed the frequencies  $F_{\text{DFT}}$  associated with the extremal cross-sectional areas for all Fermi pockets and plot them in Fig. 2(a) as black dots. Excellent agreement between  $F_{\text{DFT}}$  and  $F_{\text{dHvA}}$  is achieved in terms of both angular dependence and magnitude. We circled the sections of the Fermi pockets that correspond to  $F_{\text{DFT}}$  and labeled them as pockets A, A', B, C, and C', as shown in Fig. 2(c). The  $\alpha$ ,  $\alpha'$ , and  $\beta$  branches correspond to sheets A, A', and B,

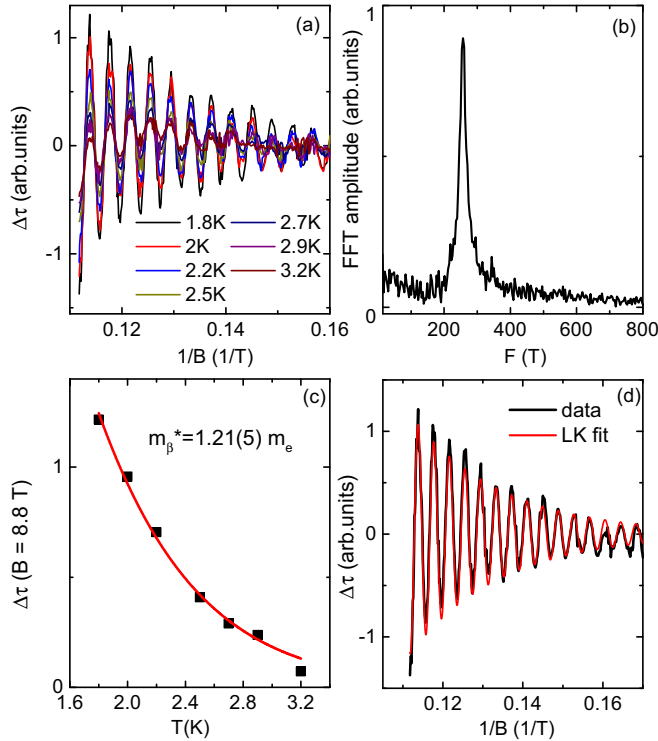


FIG. 3.  $F_\beta$  branch: (a)  $\Delta\tau$ , obtained after subtracting a polynomial background, as a function of  $1/B$  for temperatures up to 3.2 K. (b) The FFT plot of  $\Delta\tau$ , revealing one frequency at  $F_\beta = 257$  T. (c) A fit of the amplitude at a fixed magnetic field of 8.8 T to obtain the effective mass associated with the orbit. (d) Data at 1.8 K (black line) with the LK fit (red line).

respectively. A and A' are centered around the  $M$  Weyl point, and B is near the trivial  $H$  point.

We noticed that the frequency branches associated with Fermi pockets C and C' are missing from the experiment. This is, however, common. In NbAs<sub>2</sub>, for example, despite the excellent agreement between DFT and experiment, a small frequency branch is completely absent from the observed quantum oscillations [25]. If we increase the  $E_F$  by 25 meV to examine whether better agreement is possible, pockets C and C' become much larger and disappear from the frequency range shown in Fig. 2(a), but the sizes of  $F_{\text{DFT}}^A$  and  $F_{\text{DFT}}^{A'}$  become half of the experimental values. It is worth noting that in both cases  $\alpha$ ,  $\alpha'$ , and  $\beta$  correspond to pockets A, A', and B.

### B. Berry phases revealed by dHvA oscillations

In order to experimentally investigate the topology of each Fermi pocket, we rotated the sample in such a way to observe only the frequencies associated with that pocket. Figure 3(a) shows the oscillations in torque as a function of  $1/B$  after the subtraction of a polynomial background. At an angle close to  $\approx 135^\circ$  in Fig. 2(a), the FFT of the oscillations shows that only one frequency,  $F_\beta = 257$  T, is present [Fig. 3(b)].

The amplitude of the quantum oscillations can be described by the Lifshitz-Kosevich (LK) formalism. For magnetic torque measurements, the sum of the quantum oscillations

from all extremal orbits can be calculated by [26]

$$\Delta\tau \propto \pm \sum_i B^{3/2} R_T R_D R_S \sin \left[ 2\pi \left( \frac{F_i}{B} + \phi_i \right) \right]. \quad (1)$$

The choice of  $\pm$  depends on details of the Fermi surface.  $R_T$  represents the thermal damping factor, which is a finite-temperature correction to the Fermi-Dirac distribution. It dominates the temperature dependence of the oscillation amplitude and is given by the equation  $R_T = \alpha T \mu / [B \sinh(\alpha T \mu / B)]$ , where the constant  $\alpha$  is equal to 14.69 T/K and  $\mu$  is the ratio between the cyclotron effective mass  $m^*$  and the free-electron mass  $m_e$ .  $R_D = \exp(-\alpha T_D \mu / B)$  is the so-called Dingle damping factor, which is related to the quantum lifetime through the equation  $\tau_q = \hbar / (2\pi k_B T_D)$ .  $R_S = \cos(\pi g \mu / 2)$  is the spin damping factor, which accounts for the interference between two oscillations from spin-split Landau levels. The phase factor  $\phi_i$  in Eq. (1) is of particular importance because it contains information about the Berry phase of the material. It is equal to  $-(1/2 - \phi_B / 2\pi) + \delta$ , where  $\phi_B$  is the Berry phase and  $\delta$  is a phase factor that is determined by the dimensionality and curvature of the Fermi surface perpendicular to the magnetic field. Materials with a  $\phi_B$  of zero or  $2\pi$  are topologically trivial, while those with a  $\phi_B$  of  $\pi$  have nontrivial topology. For a two-dimensional Fermi surface  $\delta = 0$ , for a 3D Fermi surface  $\delta$  takes the values  $1/8$  for holes and  $-1/8$  for electrons at a maximum cross section of the Fermi surface, while it is  $1/8$  for electrons and  $-1/8$  for holes at a minimum cross section [27].

As shown in Fig. 3(a), the amplitude of the oscillations decays rapidly with temperature, suggesting that this pocket is associated with a relatively sizable effective mass. Indeed, using the expression for the thermal damping factor  $R_T$ , a fit of the amplitude at a fixed field of 8.8 T as a function of temperature results in the value  $m^* = 1.21(5)m_e$ , as shown in Fig. 3(c). Figure 3(d) shows a fit of the oscillation pattern to the LK formula with a frequency of 257 T.

Next, we investigated the topological character of the spin-split A and A' pockets. Figure 4(a) shows the FFT spectrum of the oscillations obtained when the magnetic field was applied at an angle corresponding to  $\approx 70^\circ$  in Fig. 2(a). At this angle, the effect of spin splitting can be seen very clearly without contamination from the  $\beta$  frequency. Figure 4(b) shows the temperature dependence of the FFT amplitudes of these two oscillation peaks. An effective field  $1/B_{\text{eff}} = (1/B_1 + 1/B_2)/2$  with  $B_1 = 9$  T and  $B_2 = 2.5$  T, the limits of the FFT we performed, was used to fit  $R_T$ . The effective masses associated with frequencies  $\alpha$  and  $\alpha'$  were  $0.21(1)m_e$  and  $0.24(1)m_e$ , respectively. These effective masses are much smaller than  $1.21m_e$  but still larger than those in the topological semimetal Cd<sub>3</sub>As<sub>2</sub> [28,29]. Figures 4(c)–4(e) show the fits to the LK formula in order to determine the Berry phases and quantum mobilities associated with these pockets. Since the oscillations are made up of two frequencies, we used a version of Eq. (1) with two components. We examined three different cases: that they are characterized by different phase factors and Dingle temperatures [Fig. 4(c)], that they have the same phase factors [Fig. 4(d)], and that they have the same Dingle temperatures [Fig. 4(e)]. All expressions seem to fit the data very well, and the phase factors derived from all three fits are quite robust with very similar values. However, since A and

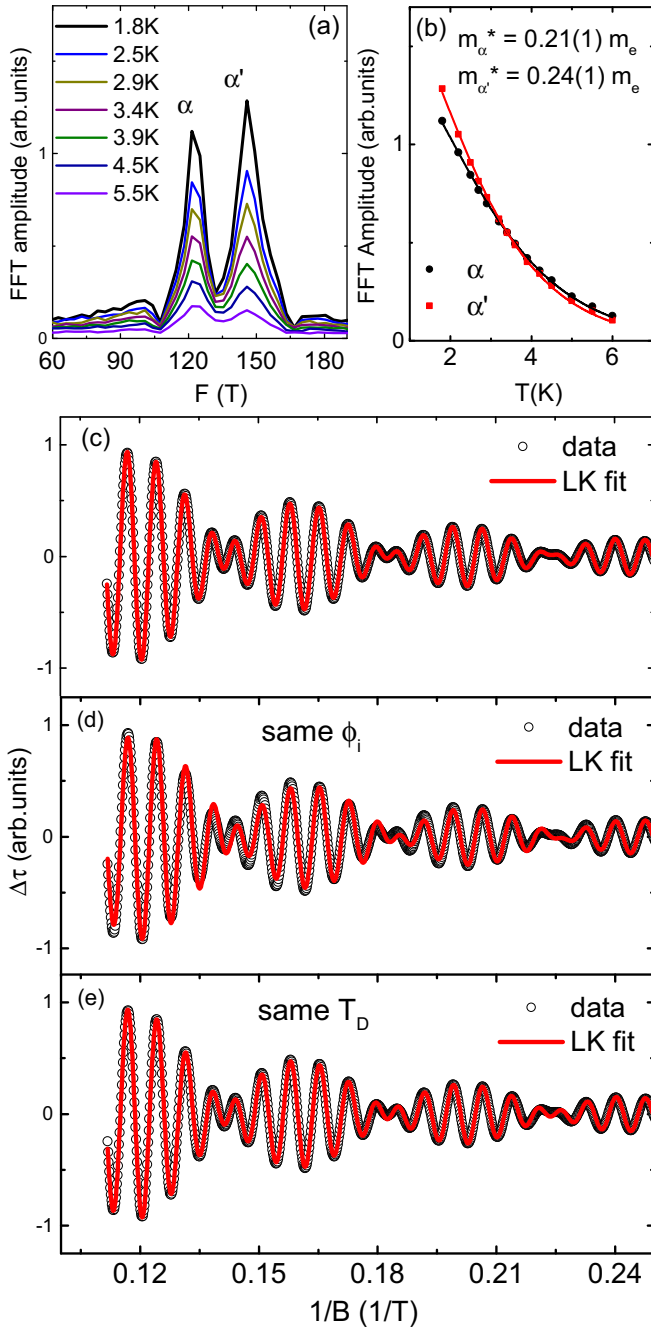


FIG. 4. (a) The FFT spectrum of the oscillations obtained with the magnetic field at an angle of  $\approx 70^\circ$  with respect to the [101] axis. (b) Fit of the temperature dependence of the FFT amplitude to determine the effective masses. (c)–(e)  $\Delta\tau$  (black line) with the LK fit with two frequencies shown in red. For both frequencies, (c)  $\phi_i$  and  $T_D$  are all free parameters; (d)  $T_D$  are free parameters, and  $\phi_i$  are set to be equal; and (e)  $\phi_i$  are free parameters, and  $T_D$  are set to be equal.

$A'$  are very similar [Fig. 2(c)], we believe that they should be characterized by the same Dingle temperatures; therefore, the values obtained in Fig. 4(e) were used.

Table I summarizes the obtained quantum lifetimes  $\tau_q$ , quantum mobilities  $\mu_q$ , and Berry phases  $\phi_B$ . It is unclear if the positive or negative sign should be used in Eq. (1), so both

situations are considered. Since all three Fermi pockets are hole pockets and the data we analyzed were collected near the minima of the extremal cross sections,  $\delta = -1/8$  was used in the calculation of the Berry phases.

A trivial Berry phase was expected for the  $\beta$  branch since Fermi pocket B is near the trivial  $H$  point. We therefore believe that the negative sign, which results in a trivial Berry phase of  $0.3(1)\pi$ , should be used. On the other hand, regardless of the choice of sign, the Berry phases calculated for the  $\alpha$  and  $\alpha'$  pockets do not allow us to conclude whether they are trivial or not. Interestingly, in a quantum oscillations study of CoSi, despite a long Fermi arc surface state being observed in angle-resolved photoemission spectroscopy measurements [30], a trivial Berry phase was observed for the electron pockets at the Kramers-Weyl point [24] because the linear dispersion region was too far from the Fermi level.

### C. Quasilinear magnetoresistance arising from open Fermi surfaces

The normal-state field-dependent MR, which was measured with  $H \parallel [101]$ , is shown in Figs. 5(a) and 5(b). It is quasilinear and quite high at low temperatures, exceeding 1000% at 2.4 K and 9 T, but decays quickly with increasing temperature. At 100 K, the highest temperature measured, the MR becomes quadratic and reaches only 1% at 9 T. The field-dependent Hall resistivity is shown in Fig. 5(c) for a few temperatures. The Hall resistivity is nonlinear, in agreement with the prediction that both hole and electron pockets are present at the Fermi level. Two-band model fitting did not work for this case due to the linear MR. To get a rough estimate of the carrier concentration, a linear fit of the Hall resistivity at 4 K gives a value of  $1.27 \times 10^{22} \text{ cm}^{-3}$ . Theoretical models for linear MR have been established for low carrier density semimetals with linear dispersions in their ultraquantum limit [31], which is clearly not the case here since 9 T is too low for NbGe<sub>2</sub> to enter this limit. Linear MR has also been proposed to be a result of the topological protection from backscattering being lifted by the applied magnetic field [28], mobility fluctuations [29], or the formation of open orbits on their Fermi surface [32].

To understand the possible cause of the linear MR, a theoretical analysis was performed. To obtain the conductivity tensor we solved the Boltzmann transport equation within the relaxation time approximation [33], as implemented in the WANNIERTOOL code suit [34,35]. The main equation of interest is

$$\sigma_{ij}^{(n)}(\mathbf{B}) = \frac{e^2}{4\pi^3} \int d\mathbf{k} \tau_n \mathbf{v}_n(\mathbf{k}) \bar{\mathbf{v}}_n(\mathbf{k}) \left( -\frac{\partial f}{\partial \varepsilon} \right)_{\varepsilon=\varepsilon_n(\mathbf{k})}, \quad (2)$$

where  $n$  is the band index,  $e$  is electronic charge,  $f$  is Fermi-Dirac distribution,  $\mathbf{v}_n(\mathbf{k})$  is the velocity obtained from the gradient of the band energy, and  $\bar{\mathbf{v}}_n(\mathbf{k})$  is the velocity averaged over the past time of the charge carrier, given by

$$\bar{\mathbf{v}}_n(\mathbf{k}) = \int_{-\infty}^0 \frac{dt}{\tau_n} e^{\frac{t}{\tau_n}} \mathbf{v}_n(\mathbf{k}(t)). \quad (3)$$

TABLE I. Effective masses, Dingle temperatures, quantum lifetimes and mobilities, and Berry phases for pockets  $\alpha$ ,  $\alpha'$ , and  $\beta$ .

	$F(T)$	$m/m_e$	$T_D$ (K)	$\tau_q$ (ps)	$\mu_q$ (cm <sup>2</sup> /V s)	Sign	$\phi_i$	$\phi_B$
$\alpha$	122	0.21	1.2	1.0	8500	+	0.06(6)	1.4(1) $\pi$
						-	0.56(6)	0.4(1) $\pi$
$\alpha'$	146	0.24	1.2	1.0	7400	+	0.08(9)	1.4(2) $\pi$
						-	0.58(9)	0.4(2) $\pi$
$\beta$	257	1.21	0.48	2.5	3700	+	0.04(4)	1.3(1) $\pi$
						-	0.53(4)	0.3(1) $\pi$

The evolution of  $\mathbf{k}_n(t)$  is caused by the orbital motion of charge carrier in the external magnetic field, given by

$$\frac{d\mathbf{k}_n(t)}{dt} = -\frac{e}{\hbar}\mathbf{v}_n(\mathbf{k}(t)) \times \mathbf{B}. \quad (4)$$

The relaxation time for different bands  $\tau_n$  is assumed to be independent of momentum, and within the relaxation time approximation we have neglected the interband scattering events. Once the conductivity tensor  $\hat{\sigma}$  was obtained, we calculated the resistivity using the equation  $\hat{\rho} = \hat{\sigma}^{-1}$ . As shown in Fig. 5(d), we can, indeed, see linear MR at low temperatures and quadratic MR at high temperatures. This calculation did not take into account SOC or a complicated anomalous velocity that could result from the Berry curvature and considered only Fermi surface effects. The agreement with our experimental results suggests that the observed linear

MR might simply arise from Fermi surface effects and is most likely due to the presence of open Fermi surfaces.

#### D. Type-I superconductivity with a full gap

The superconducting properties of NbGe<sub>2</sub> were studied using specific heat, magnetization, and resistivity measurements. The inset of Fig. 6(a) shows the low-temperature  $C_p/T$  versus  $T^2$ , with the red line corresponding to a fit of the normal-state data to the equation  $C_p = C_{el} + C_{ph} = \gamma_n T + \beta T^3$ , which results in a Sommerfeld coefficient  $\gamma_n = 6.34$  mJ/mol K<sup>-2</sup> and  $\beta = 0.05$  mJ/mol K<sup>-4</sup>. The size of the peak indicates that NbGe<sub>2</sub> is a bulk superconductor, and the sharpness of the transition highlights the excellent degree of crystallinity of our sample. The Debye temperature can be calculated from the equation  $\Theta_D = (12\pi^4 n R / 5\beta)^{1/3}$ , where  $n$  is the number of atoms in the unit cell. For NbGe<sub>2</sub>  $n = 3$ , and thus, our estimate of  $\Theta_D$  is 485 K. To estimate the electron-phonon coupling constant  $\lambda_{ep}$ , we used the McMillan formula [36]

$$\lambda_{ep} = \frac{1.04 + \mu^* \ln\left(\frac{\Theta_D}{1.45T_c}\right)}{(1 - 0.62\mu^*) \ln\left(\frac{\Theta_D}{1.45T_c}\right) - 1.04}. \quad (5)$$

Using our values for  $\Theta_D$  and  $T_c$  and using  $\mu^* = 0.13$ , a common value for intermetallic superconductors [37], we estimated  $\lambda_{ep}$  to be 0.47, suggesting weak coupling in the SC state of NbGe<sub>2</sub>. Figure 6(a) shows the electronic heat capacity divided by  $\gamma_n T_c$  as a function of the reduced temperature  $T/T_c$ .  $\Delta C_{el}/\gamma_n T_c$  was estimated to be  $\approx 1.36$ , very close to the BCS value of 1.43. The prediction of the single-band  $\alpha$  model [38], for  $\alpha = \alpha_{BCS}$ , is shown as a pink dashed line. The excellent agreement in the entire temperature range indicates that NbGe<sub>2</sub> is a fully gapped weak-coupling SC.

The hysteresis curve at 0.5 K [Fig. 6(b)] shows a typical type-II SC behavior [39]. However, the specific heat measurements under magnetic field presented in Fig. 6(c) provide strong evidence of type-I SC since the application of a magnetic field causes a sudden jump in the specific heat and thus a large latent heat even at 1.2 mT. This suggests a first-order phase transition under field, typical of type-I SCs [40,41]. To resolve this controversy, we measured several magnetization isotherms from 0.5 to 1.6 K with  $H \perp [111]$ , as shown in Fig. 6(d), and found type-II to type-I crossover behavior upon warming. This is consistent with the data shown in Fig. 6(c),

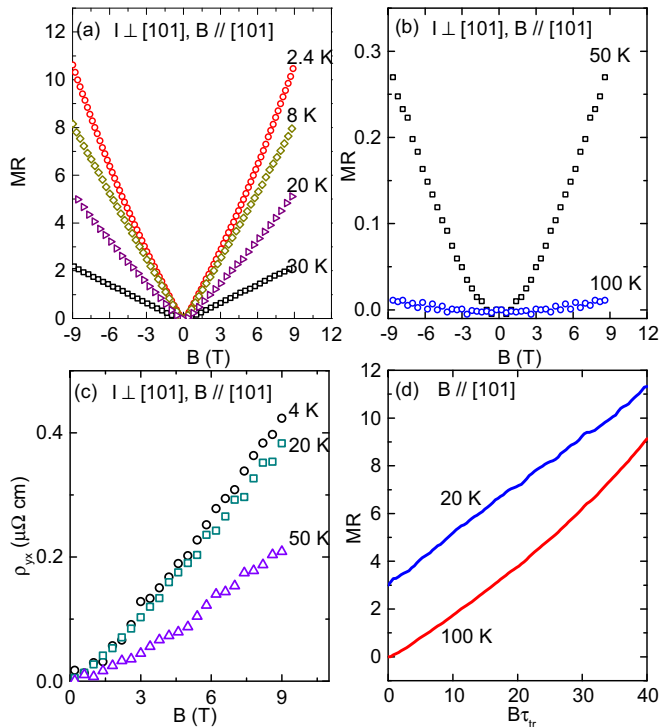


FIG. 5. (a) and (b) MR at several temperatures. (c) Hall resistivity at various temperatures. (d) The calculated MR at 20 and 100 K with offset. The calculation was done by solving the Boltzmann transport equation within the relaxation time approximation.

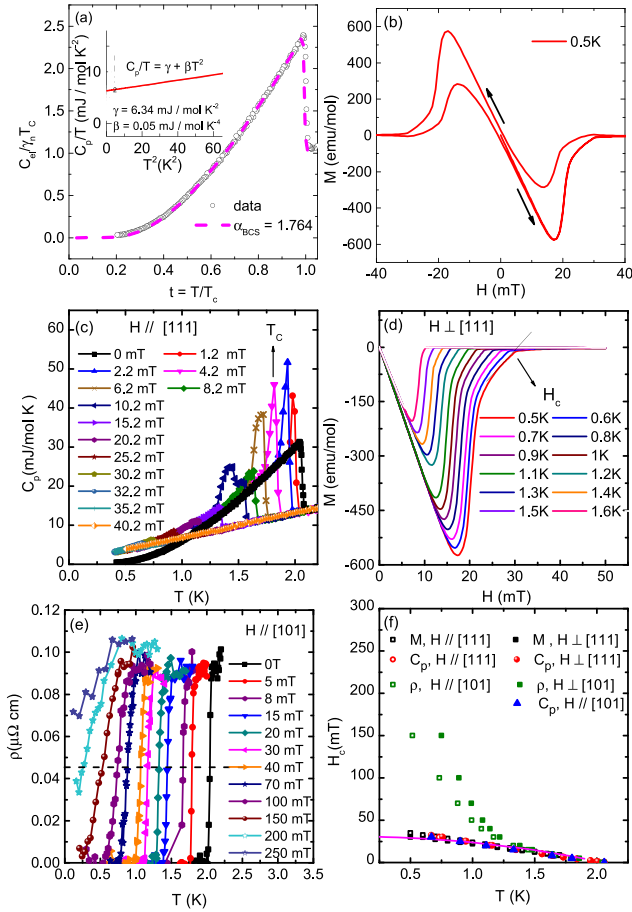


FIG. 6. (a) A comparison of the electronic part of the specific heat  $C_{el}/\gamma_n T_c$  to the predictions of the BCS model. Inset:  $C_p/T$  as a function of  $T^2$ , with a fit to  $C_p/T = \gamma + \beta T^2$ . (b)  $M$ - $H$  loop at 0.5 K. (c) Specific heat with  $H \parallel [111]$  at various fields. (d) Magnetic isotherms with  $H \perp [111]$  at several temperatures. (e) Resistivity under various fields with  $H \parallel [101]$ . The dashed line indicates where  $\rho$  has decreased to 50% of its value since the onset of the transition and was used to determine  $T_c$  at each field. (f)  $H$ - $T$  phase diagram, with values determined from specific heat, magnetic susceptibility, and resistivity measurements. The purple line corresponds to a fit to the expression  $H_c(T) = H_c(0)[1 - (T/T_c)^2]$ .

where the latent heat was observed only above 1.5 K, suggesting type-I SC above 1.5 K and type-II SC below 1.5 K.

The  $H$ - $T$  phase diagram is presented in Fig. 6(f) using data from all three types of measurements. The thermodynamic critical fields extracted from magnetization and specific heat can be fit to the BCS expression  $H_c(T) = H_c(0)[1 - (T/T_c)^2]$ , resulting in the value  $H_c(0) = 30.9(5)$  mT. However, the critical fields we obtained using resistivity data show distinct behavior [Fig. 6(e)]. Although a different field direction was used, above 1.3 K, all critical fields are in good agreement, suggesting isotropic superconductivity. Below 1.3 K, however, the critical fields extracted from resistivity measurements show a steep upturn leading to an extrapolated  $H_c(0)$  around 10 times greater than that obtained from the other two measurements. To ensure that this upturn is not associated with the [101] direction, we also measured specific heat with  $H \parallel [101]$ . The critical fields obtained from

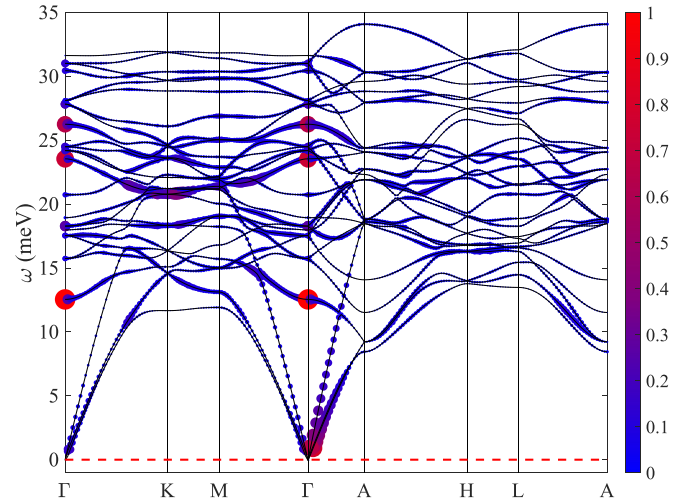


FIG. 7. (a) The electron-phonon coupling weighted phonon band structure of NbGe<sub>2</sub>. The size and color of each marker denotes the mode and wave-vector-resolved electron-phonon coupling. The color bar denotes the value of the electron-phonon coupling.

this measurement are in good agreement with those extracted from the rest of the specific heat and magnetization measurements and show no upturn of  $H_c$ . The fact that this upturn is missing from the specific heat and magnetization data could indicate the presence of filamentary superconductivity. It has also been observed in other NCSs, such as AuBe, LaRhSi<sub>3</sub>, and BiPd [42–44]. The nontrivial band topology that has been proposed by DFT calculations for NbGe<sub>2</sub>, AuBe, and BiPd raises the question of whether the upturn of  $H_c$  could be related to nontrivial topology. Could it be indicative of the topological surface superconductivity which arises from the proximity effect of bulk superconductivity and surface topological electrons, like the one proposed in FeTe<sub>1-x</sub>Se<sub>x</sub> ( $x = 0.45$ ) and PbTaSe<sub>2</sub> [45,46]? Further theoretical work is necessary to address this interesting and apparently common behavior in NCSs.

To understand the possible origin and nature of the superconductivity in NbGe<sub>2</sub>, we calculated the phonon mode and wave-vector-resolved electron-phonon coupling using the EPW code [47,48],

$$\lambda_{\mathbf{q}\nu} = \frac{\gamma_{\mathbf{q}\nu}}{\pi N(\varepsilon_F)\omega_{\mathbf{q}\nu}^2}, \quad (6)$$

where  $\mathbf{q}$  is the wave vector,  $\nu$  is the phonon branch index,  $N(\varepsilon_F)$  is the electron density at the Fermi energy  $\varepsilon_F$ , and  $\omega_{\mathbf{q}\nu}$  is the phonon frequency. The phonon linewidth (imaginary part of the phonon self-energy)  $\gamma_{\mathbf{q}\nu}$  was obtained from

$$\gamma_{\mathbf{q}\nu} = 2\pi\omega_{\mathbf{q}\nu} \sum_{nm} \int_{\text{BZ}} \frac{d\mathbf{k}}{\Omega_{\text{BZ}}} |g_{mn,\nu}(\mathbf{k}, \mathbf{q})|^2 \times \delta(\varepsilon_{n\mathbf{k}} - \varepsilon_F)\delta(\varepsilon_{m\mathbf{k}+\mathbf{q}} - \varepsilon_F), \quad (7)$$

where  $g_{mn,\nu}(\mathbf{k}, \mathbf{q})$  is the electron-phonon matrix element and  $m, n$  are the electronic band indices. The phonon mode and wave-vector-resolved electron-phonon coupling for NbGe<sub>2</sub> are shown in Fig. 7, where the size and color of the points depict the weight of the electron-phonon coupling. We found

that the modes near the high-symmetry point  $\Gamma$  along the  $\Gamma$ -A direction have the highest contributions. We have further calculated the total electron-phonon coupling from the BZ average of the mode-resolved electron-phonon coupling by using  $\lambda_{\text{eq}} = \sum_{\text{q}\nu} w_{\text{q}\nu} \lambda_{\text{q}\nu}$ . Our calculation results in  $\lambda_{\text{ep}} = 0.67$ , which is 30% larger than 0.47, the experimentally obtained value. To estimate  $T_c$ , we used the value of  $\lambda_{\text{ep}} = 0.67$  with the Allen-Dynes formula

$$T_c = \frac{\omega_{\text{log}}}{1.2} \exp \left[ \frac{-1.04(1 + \lambda_{\text{ep}})}{\lambda_{\text{ep}}(1 - 0.62\mu^*) - \mu^*} \right]. \quad (8)$$

For a screened Coulomb interaction parameter of  $\mu^* = 0.13$  or 0.16,  $T_c$  is estimated to be  $\approx 5.4$  and 3.8 K, respectively, comparable to the experimental value. This suggests that the SC in NbGe<sub>2</sub> is, indeed, electron-phonon mediated.

#### IV. CONCLUSION

In summary, we have investigated the fermiology, magnetotransport, and SC properties in the chiral SC NbGe<sub>2</sub>. The angular dependence and magnitude of the quantum oscillations are in excellent agreement with the DFT calculations, suggesting that the observed frequencies  $\beta$  and  $\alpha/\alpha'$  are associated with the hole Fermi pockets centered near the trivial  $H$  point and the Weyl  $M$  point, respectively. An analysis of the quantum oscillations suggests a trivial Berry phase for  $\beta$  and Berry phases close to  $0.4\pi$  for  $\alpha$  and  $\alpha'$ , most likely because

the Fermi level is located 0.05 eV away from the Kramers-Weyl node, where only a small linear dispersion region exists. We attribute the observed electron-phonon mediated SC to the Van Hove singularity arising from the saddle-point-like dispersion at the  $M$  and  $H$  points near the Fermi level.

*Note added.* Recently, we became aware of a publication on the superconducting properties of NbGe<sub>2</sub> [49] which are consistent with our results. That publication, however, did not contain the presentation and analysis of either the fermiology or the magnetotransport in NbGe<sub>2</sub>.

#### ACKNOWLEDGMENTS

Work at UCLA was supported by the NSF DMREF program under NSF DMREF Project No. DMREF-1629457. T.-R.C. was supported by the Young Scholar Fellowship Program from the Ministry of Science and Technology (MOST) in Taiwan, under a MOST grant for the Columbus Program, Grant No. MOST108-2636-M-006-002; National Cheng Kung University, Taiwan; and the National Center for Theoretical Sciences, Taiwan. This work was supported partially by the MOST, Taiwan, under Grant No. MOST107-2627-E-006-001. This research was supported, in part, by the Higher Education Sprout Project, Ministry of Education to the Headquarters of University Advancement at National Cheng Kung University (NCKU). The work at IIT Kanpur benefited from the high-performance facilities of the computer center of IIT Kanpur.

- 
- [1] D. Hsieh, Y. Xia, D. Qian, L. Wray, J. H. Dil, F. Meier, J. Osterwalder, L. Patthey, J. G. Checkelsky, N. P. Ong, A. V. Fedorov, H. Lin, A. Bansil, D. Grauer, Y. S. Hor, R. J. Cava, and M. Z. Hasan, *Nature (London)* **460**, 1101 (2009).
- [2] D. Hsieh, Y. Xia, L. Wray, D. Qian, A. Pal, J. H. Dil, J. Osterwalder, F. Meier, G. Bihlmayer, C. L. Kane, Y. S. Hor, R. J. Cava, and M. Z. Hasan, *Science* **323**, 919 (2009).
- [3] S. M. Young, S. Zaheer, J. C. Y. Teo, C. L. Kane, E. J. Mele, and A. M. Rappe, *Phys. Rev. Lett.* **108**, 140405 (2012).
- [4] J. Nayak, S.-C. Wu, N. Kumar, C. Shekhar, S. Singh, J. Fink, E. E. D. Rienks, G. H. Fecher, S. S. P. Parkin, B. Yan, and C. Felser, *Nat. Commun.* **8**, 13942 (2017).
- [5] S.-M. Huang, S.-Y. Xu, I. Belopolski, C.-C. Lee, G. Chang, B. Wang, N. Alidoust, G. Bian, M. Neupane, C. Zhang, S. Jia, A. Bansil, H. Lin, and M. Z. Hasan, *Nat. Commun.* **6**, 7373 (2015).
- [6] S. Jia, S.-Y. Xu, and M. Z. Hasan, *Nat. Mater.* **15**, 1140 (2016).
- [7] G. B. Osterhoudt, L. K. Diebel, M. J. Gray, X. Yang, J. Stanco, X. Huang, B. Shen, N. Ni, P. J. W. Moll, Y. Ran, and K. S. Burch, *Nat. Mater.* **18**, 471 (2019).
- [8] G. Chang, B. J. Wieder, F. Schindler, D. S. Sanchez, I. Belopolski, S.-M. Huang, B. Singh, D. Wu, T.-R. Chang, T. Neupert, S.-Y. Xu, H. Lin, and M. Z. Hasan, *Nat. Mater.* **17**, 978 (2018).
- [9] C. M. Knodler and D. H. Douglass, *J. Low Temp. Phys.* **37**, 189 (1979).
- [10] J. P. Remeika, A. S. Cooper, Z. Fisk, and D. C. Johnston, *J. Less-Common Met.* **62**, 211 (1978).
- [11] M. Smidman, M. B. Salamon, H. Q. Yuan, and D. F. Agterberg, *Rep. Prog. Phys.* **80**, 036501 (2017).
- [12] W. Xie, P. Zhang, B. Shen, W. Jiang, G. Pang, T. Shang, C. Cao, M. Smidman, and H. Yuan, *Sci. China Phys., Mech. Astron.* **63**, 237412 (2020).
- [13] B. Li, C. Q. Xu, W. Zhou, W. H. Jiao, R. Sankar, F. M. Zhang, H. H. Hou, X. F. Jiang, B. Qian, B. Chen, A. F. Bangura, and X. Xu, *Sci. Rep.* **8**, 651 (2018).
- [14] P. Hohenberg and W. Kohn, *Phys. Rev.* **136**, B864 (1964).
- [15] W. Kohn and L. J. Sham, *Phys. Rev.* **140**, A1133 (1965).
- [16] P. E. Blöchl, *Phys. Rev. B* **50**, 17953 (1994).
- [17] G. Kresse and J. Furthmüller, *Phys. Rev. B* **54**, 11169 (1996).
- [18] G. Kresse and D. Joubert, *Phys. Rev. B* **59**, 1758 (1999).
- [19] J. P. Perdew, K. Burke, and M. Ernzerhof, *Phys. Rev. Lett.* **77**, 3865 (1996).
- [20] H. J. Monkhorst and J. D. Pack, *Phys. Rev. B* **13**, 5188 (1976).
- [21] N. Marzari and D. Vanderbilt, *Phys. Rev. B* **56**, 12847 (1997).
- [22] J. L. Jorda, R. Flükiger, and J. Müller, *J. Less-Common Met.* **62**, 25 (1978).
- [23] H. Tsutsumi, Y. Miura, H. Harima, F. Honda, and Y. Onuki, *J. Phys. Soc. Jpn.* **82**, 094604 (2013).
- [24] X. Xu, X. Wang, T. A. Cochran, D. S. Sanchez, G. Chang, I. Belopolski, G. Wang, Y. Liu, H.-J. Tien, X. Gui, W. Xie, M. Z. Hasan, T.-R. Chang, and S. Jia, *Phys. Rev. B* **100**, 045104 (2019).
- [25] B. Shen, X. Deng, G. Kotliar, and N. Ni, *Phys. Rev. B* **93**, 195119 (2016).

- [26] J. Liu, P. Liu, K. Gordon, E. Emmanouilidou, J. Xing, D. Graf, B. C. Chakoumakos, Y. Wu, H. Cao, D. Dessau, Q. Liu, and N. Ni, *Phys. Rev. B* **100**, 195123 (2019).
- [27] C. Li, C. M. Wang, B. Wan, X. Wan, H.-Z. Lu, and X. C. Xie, *Phys. Rev. Lett.* **120**, 146602 (2018).
- [28] T. Liang, Q. Gibson, M. N. Ali, M. Liu, R. J. Cava, and N. P. Ong, *Nat. Mater.* **14**, 280 (2015).
- [29] A. Narayanan, M. D. Watson, S. F. Blake, N. Bruyant, L. Drigo, Y. L. Chen, D. Prabhakaran, B. Yan, C. Felser, T. Kong, P. C. Canfield, and A. I. Coldea, *Phys. Rev. Lett.* **114**, 117201 (2015).
- [30] D. S. Sanchez *et al.*, *Nature (London)* **567**, 500 (2019).
- [31] A. A. Abrikosov, *Phys. Rev. B* **58**, 2788 (1998).
- [32] B. Wu, V. Barrena, H. Suderow, and I. Guillamón, *Phys. Rev. Research* **2**, 22042(R) (2020).
- [33] N. W. Ashcroft and N. D. Mermin, *Solid State Physics* (Cornell University, Ithaca, NY, 1976).
- [34] Q. Wu, S. Zhang, H.-F. Song, M. Troyer, and A. A. Soluyanov, *Comput. Phys. Commun.* **224**, 405 (2018).
- [35] S. N. Zhang, Q. S. Wu, Y. Liu, and O. V. Yazyev, *Phys. Rev. B* **99**, 035142 (2019).
- [36] W. L. McMillan, *Phys. Rev.* **167**, 331 (1968).
- [37] D. Singh, J. A. T. Barker, A. Thamizhavel, A. D. Hillier, D. M. Paul, and R. P. Singh, *J. Phys.: Condens. Matter* **30**, 075601 (2018).
- [38] D. C. Johnston, *Supercond. Sci. Technol.* **26**, 115011 (2013).
- [39] H. ElBidweihy, *AIP Adv.* **6**, 056402 (2016).
- [40] E. Svanidze and E. Morosan, *Phys. Rev. B* **85**, 174514 (2012).
- [41] D. C. Peets, E. Cheng, T. Ying, M. Kriener, X. Shen, S. Li, and D. Feng, *Phys. Rev. B* **99**, 144519 (2019).
- [42] D. J. Rebar, S. M. Birnbaum, J. Singleton, M. Khan, J. C. Ball, P. W. Adams, J. Y. Chan, D. P. Young, D. A. Browne, and J. F. DiTusa, *Phys. Rev. B* **99**, 094517 (2019).
- [43] N. Kimura, H. Ogi, K. Satoh, G. Ohsaki, K. Saitoh, H. Iida, and H. Aoki, *JPS Conf. Proc.* **3**, 015011 (2014).
- [44] M. Khan, Ph.D. thesis, Louisiana State University, 2017.
- [45] P. Zhang, K. Yaji, T. Hashimoto, Y. Ota, T. Kondo, K. Okazaki, Z. Wang, J. Wen, G. D. Gu, H. Ding, and S. Shin, *Science* **360**, 182 (2018).
- [46] T.-R. Chang, P.-J. Chen, G. Bian, S.-M. Huang, H. Zheng, T. Neupert, R. Sankar, S.-Y. Xu, I. Belopolski, G. Chang, B. K. Wang, F. Chou, A. Bansil, H.-T. Jeng, H. Lin, and M. Z. Hasan, *Phys. Rev. B* **93**, 245130 (2016).
- [47] E. R. Margine and F. Giustino, *Phys. Rev. B* **87**, 024505 (2013).
- [48] S. Poncé, E. R. Margine, C. Verdi, and F. Giustino, *Comput. Phys. Commun.* **209**, 116 (2016).
- [49] B. Lv, M. Li, J. Chen, Y. Yang, S. Wu, L. Qiao, F. Guan, H. Xing, Q. Tao, G.-H. Cao, and Z.-A. Xu, *Phys. Rev. B* **102**, 064507 (2020).